The effect of airfoil elasticity on quasistatic aerodynamics and divergence

Netanel Chen [*], Amir D. Gat (Ph.D. Assoc. Prof.)

The Faculty of Mechanical Engineering, Technion - Israel Institute of Technology (IIT), Haifa 32000, Israel

ARTICLE INFO

ABSTRACT

Shape-morphing airfoils are of interest due to their benefits for aerodynamic efficiency and commonly involve chordwise elasticity of the airfoil. We aim to examine the influence of chordwise elasticity on the aerodynamic properties and stability in the quasistatic limit. We model a shape-morphing airfoil as two, rear and front, Euler–Bernoulli beams connected to a rigid support at an arbitrary location along its chord. This setup is mounted on a torsion spring and is exposed to a uniform flow. We model aerodynamic forces acting on the wing via thin airfoil theory and obtain the solution of the elastic deflection via regular asymptotic expansions. Then, we substitute this result into the moment balance equation to find the rotation angle. This procedure allows us to examine the influence of chord-wise elasticity on the lift, aerodynamic center, twist angle, and the onset of divergence. We examine these results in terms of the elastic axis location and the dimensionless ratio between aerodynamic moment to bending stiffness. The lift curve slope is smaller than 2π up to the hinge location of about 0.53 chord and is greater than 2π elsewhere. The chord-wise elasticity moves the aerodynamic center forwards and increases the twist angle. In addition, chord-wise elasticity is found to increase the onset of divergence relative to the rigid case. Moreover, unlike the rigid case, divergence also exists for hinges in the front quarter chord. Finally, we present several possible cases of an actuated airfoil validated by numerical simulations.

© 2023 Elsevier Ltd. All rights reserved.

1. Introduction

Quasistatic aeroelasticity is concerned with physical phenomena which include an interaction of aerodynamic and elastic forces. The classic literature commonly uses a simplified aeroelastic model consisting of a rigid airfoil mounted on a torsional spring. The spring stiffness represents the supporting beam's span-wise elasticity. In recent years, various researchers studied the effects of chord-wise aeroelasticity, which is common in biology, energy harvesting, and in the context of morphing airfoils (meaning wings sections that change their shape continuously) (MacPhee and Beyene, 2016; Tang and Dowell, 2018; Tiomkin and Raveh, 2017). Currently, shape-morphing airfoils are studied due to their potential to enhance the performance of aircraft structures and energy harvesting systems (see Moosavian et al., 2017; Nguyen et al., 2015; Takahashi et al., 2016, among others).

There are many approaches in the literature to fabricate wings with shape-morphing capabilities. These include piezoelectric actuation, shape memory alloys, pneumatic artificial muscles, and deployable and foldable structures (see detailed discussions in Barbarino et al., 2011; Thill et al., 2008 and references therein). The realization of shape-morphing

---

* Corresponding author.
E-mail addresses: netanel@campus.technion.ac.il (N. Chen), amirgat@technion.ac.il (A.D. Gat).
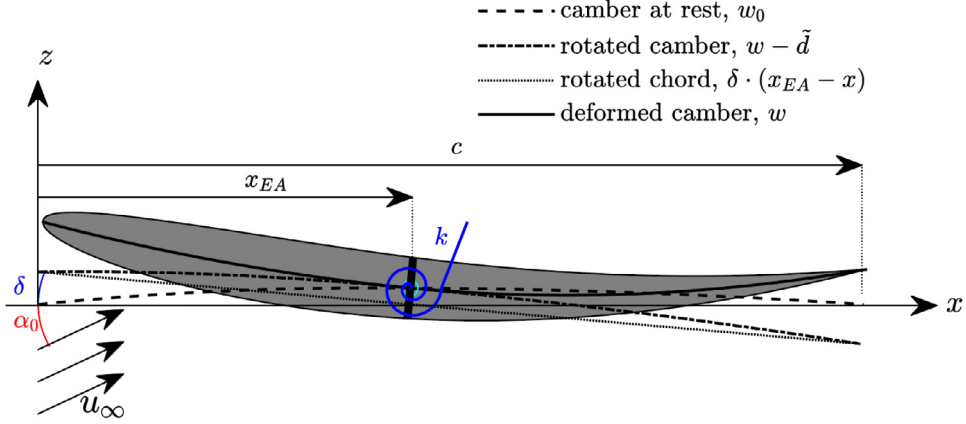
Fig. 1. Illustration of the examined configuration. w_0 (dashed line) is the airfoil's camber at rest. The dotted line represents the rotation of the chord by δ, so that the dashed–dotted line is the undeformed rotated camber. w (solid line) is the total camber (including elastic deformations). The black rectangle and blue spiral represent the support beam, located at the elastic axis x_{EA}, and its span-wise rotational stiffness, k. The airfoil is sufficiently thin to allow the use of the thin airfoil theory and Euler–Bernoulli beam approximations. . (For interpretation of the references to color in this figure legend, the reader is referred to the web version of this article.)

airfoils is commonly accompanied by reduced chord-wise rigidity, which may dominate the aeroelastic response of the structure for sufficiently soft airfoils. Various (mainly numerical) studies examined the wings' dynamic response and stability for flags in uniform flow (Alben, 2015, 2008; Eloy et al., 2008; Manela and Howe, 2009; Mougel et al., 2016), inverted flag (Gilmanov et al., 2015; Gurugubelli and Jaiman, 2015; Kim et al., 2013; Sader et al., 2016a,b), or membrane configurations, which provide greater lift and better lift slopes (Buoso and Palacios, 2015).

In this work, we aim to analyze the effects of chord-wise elasticity on classic calculations of airfoils in potential flow. We achieve this by modeling this configuration as two cantilever beams, coupling elastic deformations with aerodynamic forces obtained by thin airfoil theory, and introducing a general actuation term into the governing equation. The presented results provide a theoretical framework for the quasistatic properties of shape-morphing soft airfoils.

2. Problem formulation and scaling

We examine the stability and quasistatic response of an elastic two-dimensional airfoil in external potential laminar flow. The airfoil's elastic deformation is modeled by the Euler–Bernoulli equation, which is coupled to aerodynamic forces calculated by thin wing theory. This approach is traditionally justified under the assumption of small camber fluctuations during the motion of the airfoil, as well as a small airfoil thickness ratio (see, for example, Dowell, 1974).

The examined configuration is illustrated in Fig. 1. We denote $w_0(x)$ as the camber at rest, $d_e(x)$ as the elastic deformation due to aerodynamic forces and $d_a(x)$ as the forced actuation of the elastic airfoil, total deformation from the initial state is $d(x) = d_e(x) + d_a(x)$ and total camber is $w(x) = w_0(x) + d(x)$. Chord-length is denoted by c, and the x-coordinate is defined by the edges of the camber at rest so that $w_0(0) = w_0(c) = 0$.

The airfoil is mounted on a torsional spring with a constant k at the elastic axis, which is located at an arbitrary point $x = x_{EA}$. The total aerodynamic angle-of-attack, α, is the sum of the initial angle-of-attack (untwisted spring) α_0, plus the increment due to elastic twist, δ,

$$\alpha = \alpha_0 + \delta. \tag{1}$$

Therefore, the velocity far from the airfoil is $(u_\infty \cos(\alpha_0), u_\infty \sin(\alpha_0))$, and the total displacement is defined as the superposition of rigid body rotation and elastic deflection $\tilde{d}$, viz

$$d(x) = \delta \cdot (x_{EA} - x) + \tilde{d}(x). \tag{2}$$

The elastic deformation of the airfoil can be described by the Euler–Bernoulli equation

$$\frac{\mathrm{d}^2}{\mathrm{d}x^2}\left[s \frac{\mathrm{d}^2}{\mathrm{d}x^2}(w - w_0 - d_a) \right] = \Delta p, \tag{3a}$$

where s denotes stiffness per unit length, and Δp is the quasi-steady aerodynamic load, given by (Johnston, 2004)

$$\Delta p = 4q_\infty \left\{ \left[\alpha_0 - \frac{1}{\pi} \int_0^\pi \frac{\mathrm{d}w}{\mathrm{d}x}\mathrm{d}\varphi \right] \cot\left(\frac{\theta}{2}\right) + \sum_{n=1}^\infty \left[\frac{2}{\pi} \int_0^\pi \frac{\mathrm{d}w}{\mathrm{d}x} \cos(n\varphi)\,\mathrm{d}\varphi \right] \sin(n\theta) \right\}, \tag{3b}$$

where $q_\infty = \rho_\infty u_\infty^2 / 2$ is the freestream dynamic pressure, and the auxiliary coordinate θ (and similarly φ) is defined by $x = c \left[1 - \cos(\theta) \right] / 2$. In addition to the elastic equation, a moment balance must be satisfied. Writing the moment balance w.r.t. x_{EA} ($\circlearrowleft$) is giving

$$k\delta = \int_0^c (x_{EA} - x)\, \Delta p\, \mathrm{d}x. \tag{3c}$$

For convenience, we henceforward use the following shortening notations. The first is

$$\mathcal{L}\langle F \rangle (\theta) = \left[-\frac{1}{\pi} \int_0^\pi (F)_\varphi\, \mathrm{d}\varphi \right] \cot\left(\frac{\theta}{2}\right) + \sum_{n=1}^\infty \left[\frac{2}{\pi} \int_0^\pi (F)_\varphi \cos(n\varphi)\, \mathrm{d}\varphi \right] \sin(n\theta), \tag{4a}$$

for an aerodynamic **load** (spatial function of coordinate θ) due to slope F, and

$$\mathcal{M}_{x_{EA}}\langle F \rangle = \int_0^\pi \left[\cos(\theta) - \cos(\theta_c) \right] \mathcal{L}\langle F \rangle (\theta) \sin(\theta)\, \mathrm{d}\theta, \tag{4b}$$

for an aerodynamic **moment** about x_{EA} due to slope F.

Hereafter, uppercase letters denote normalized variables, and asterisk superscripts denote characteristic values (i.e., the normalized function F, is defined by $F = f/f^*$, where f^* is the characteristic value of the dimensional function f). We define the normalized axial coordinate $X = x/c$, normalized camber at rest $W_0 = w_0/w_0^*$, normalized total elastic deflection and due to actuation $D = \tilde{d}/\tilde{d}^*$ and $D_a = d_a/\tilde{d}^*$, normalized initial angle-of-attack $\tilde{\alpha}_0 = \alpha_0/\alpha_0^*$ and rotation angle $\Delta = \delta/\delta^*$, normalized dynamic pressure $Q_\infty = q_\infty/q_\infty^*$, normalized elastic bending stiffness $S = s/s^*$ and rotational spring stiffness $K = k/k^*$.

Substituting normalized variables, along with (1) and (2) into (3), the order-of-magnitude analysis yields

$$\alpha_0^*, \delta^* \sim \frac{s^* \tilde{d}^*}{4 q_\infty^* c^4}, \quad k^* \sim q_\infty^* c^2. \tag{5}$$

Hence, using the shortening notations (4), the normalized governing integrodifferential equations are

$$\frac{\mathrm{d}^2}{\mathrm{d}X^2}\left[S \frac{\mathrm{d}^2}{\mathrm{d}X^2}(D - D_a) \right] = Q_\infty \left[(\tilde{\alpha}_0 + \Delta) \cot\left(\frac{\theta}{2}\right) + \Pi \mathcal{L}\left\langle \frac{\mathrm{d}W_0}{\mathrm{d}X} \right\rangle (\theta) + \varepsilon \mathcal{L}\left\langle \frac{\mathrm{d}D}{\mathrm{d}X} \right\rangle (\theta) \right], \tag{6a}$$

and

$$\left[K - 2\pi \left(X_{EA} - \frac{1}{4} \right) Q_\infty \right] \Delta = Q_\infty \left\{ 2\pi \tilde{\alpha}_0 \left(X_{EA} - \frac{1}{4} \right) + \Pi \mathcal{M}_{X_{EA}}\left\langle \frac{\mathrm{d}W_0}{\mathrm{d}X} \right\rangle + \varepsilon \mathcal{M}_{X_{EA}}\left\langle \frac{\mathrm{d}D}{\mathrm{d}X} \right\rangle \right\}, \tag{6b}$$

where Π is a dimensionless ratio, represents aerodynamic forces due to camber curvature at rest, scaled by elastic bending forces, which are defined by

$$\Pi = \frac{4 q_\infty^* c^3 w_0^*}{s^* \tilde{d}^*}. \tag{6c}$$

The additional parameter, ε, represents the ratio of aerodynamic forces due to camber deformation, scaled by elastic bending forces,

$$\varepsilon = \frac{4 q_\infty^* c^3}{s^*}. \tag{6d}$$

In the limit of small **elastic** deformations (coherent with EB beam assumptions), $\varepsilon \ll 1$.

The governing integrodifferential equation (6a) is supplemented by zero deflection and zero slope boundary conditions at X_{EA},

$$(D - D_a)|_{X_{EA}} = \left. \frac{\mathrm{d}(D - D_a)}{\mathrm{d}X} \right|_{X_{EA}} = 0, \tag{7a}$$

as well as by zero moment and zero shear at $X = 0$ and $X = 1$,

$$\left. \frac{\mathrm{d}^2(D - D_a)}{\mathrm{d}X^2} \right|_{X_b} = \left. \frac{\mathrm{d}}{\mathrm{d}X}\left[S(X) \frac{\mathrm{d}^2(D - D_a)}{\mathrm{d}X^2} \right] \right|_{X_b} = 0, \quad X_b \in \{0, 1\}. \tag{7b}$$

3. Results

We derive the solution for the final airfoil configuration (rigid-body rotation and elastic deflection) by solving the elastic equation for an arbitrary Δ and substituting the solution D in the moment balance equation (6b). Thus, we express Δ as a function of the problem's parameters.

3.1. Elastic equation solution

To overcome the complexity of the integrodifferential equation, we expand the elastic deformations asymptotically, using the small parameter defined in (6d),

$$D = \sum_{n=0}^{\infty} \varepsilon^n D_n. \tag{8}$$

Substituting the expansion into (6a), yields the leading-order equation governing D_0

$$\frac{\mathrm{d}^2}{\mathrm{d}X^2}\left[S \frac{\mathrm{d}^2}{\mathrm{d}X^2}(D_0 - D_a)\right] = Q_\infty \left[(\tilde{\alpha}_0 + \Delta)\cot\left(\frac{\theta}{2}\right) + \Pi\mathcal{L}\left\langle \frac{\mathrm{d}W_0}{\mathrm{d}X}\right\rangle(\theta)\right], \tag{9a}$$

and higher-order $O(\varepsilon^n)$ equations governing D_n are given by

$$\frac{\mathrm{d}^2}{\mathrm{d}X^2}\left[S \frac{\mathrm{d}^2 D_n}{\mathrm{d}X^2}\right] = Q_\infty \mathcal{L}\left\langle \frac{\mathrm{d}D_{n-1}}{\mathrm{d}X}\right\rangle(\theta). \tag{9b}$$

Thus, we convert the single integrodifferential equation into ordinary differential equations. The leading-order boundary conditions for D_0 are identical to (7). Higher-order equations are supplemented by the homogeneous boundary conditions

$$D_n|_{X_{EA}} = \left.\frac{\mathrm{d}D_n}{\mathrm{d}X}\right|_{X_{EA}} = \left.\frac{\mathrm{d}^2 D_n}{\mathrm{d}X^2}\right|_{X_b} = \left.\frac{\mathrm{d}}{\mathrm{d}X}\left[S\frac{\mathrm{d}^2 D_n}{\mathrm{d}X^2}\right]\right|_{X_b} = 0, \quad X_b \in \{0, 1\}. \tag{10}$$

Since the integrals in (9a) depend on known terms, D_0 may be computed by direct integration with respect to X. Due to the clamping condition at $X = X_{EA}$, (7a), the airfoil curvature is discontinuous, while the slope is continuous. Applying the boundary conditions at the free-ends, (7b) the leading-order curvature of elastic deflection is obtained. Dividing it by $S(X)$, integrating and applying (7a), we obtain the leading-order normalized slope as the linear combination of each contribution to it, shortly denoted as

$$\frac{\mathrm{d}D_0}{\mathrm{d}X} = \frac{Q_\infty}{4}(\tilde{\alpha}_0 + \Delta)\mathcal{A}(\theta) + \frac{Q_\infty}{4}\Pi\mathcal{F}\left\{ \frac{\mathrm{d}W_0}{\mathrm{d}X}\right\}(\theta) + \frac{\mathrm{d}D_a}{\mathrm{d}X}. \tag{11}$$

The explicit expressions for the spatial functions in θ, $\mathcal{A}$ and $\mathcal{F}$, are given in Eqs. (A.1) to (A.3) in Appendix A. Using this writing convention, higher-orders solutions thence can be written as

$$\frac{\mathrm{d}D_n}{\mathrm{d}X} = \frac{Q_\infty}{4}\mathcal{F}\left\{ \frac{\mathrm{d}D_{n-1}}{\mathrm{d}X}\right\}(\theta), \tag{12a}$$

which may be readily generalized into

$$\frac{\mathrm{d}D_n}{\mathrm{d}X} = \left(\frac{Q_\infty}{4}\right)^m \mathcal{F}^{(m)}\left\{ \frac{\mathrm{d}D_{n-m}}{\mathrm{d}X}\right\}(\theta), \quad \forall n \geq m. \tag{12b}$$

3.2. Influence of chord-wise elasticity on span-wise twist

We substitute the solution for D in the moment balance Eq. (6b). That way, Δ can be extracted as a function of the known parameters of the problem. Upon substitution,

$$\Delta = \frac{\left[2\pi\left(X_{EA} - \frac{1}{4}\right) + \frac{\varepsilon Q_\infty}{4}\mathcal{M}_{X_{EA}}\langle S\langle\mathcal{A}\rangle\rangle\right]\tilde{\alpha}_0 + \mathcal{M}_{X_{EA}}\left\langle\left[\frac{\mathrm{d}W_0}{\mathrm{d}X} + \frac{\varepsilon Q_\infty}{4}S\left\langle\mathcal{F}\left\{\frac{\mathrm{d}W_0}{\mathrm{d}X}\right\}\right\rangle\right]\Pi + \varepsilon S\left\langle\frac{\mathrm{d}D_a}{\mathrm{d}X}\right\rangle\right\rangle}{K/Q_\infty - 2\pi\left(X_{EA} - \frac{1}{4}\right) - \frac{\varepsilon Q_\infty}{4}\mathcal{M}_{X_{EA}}\langle S\langle\mathcal{A}\rangle\rangle}, \tag{13a}$$

where S is short for

$$S\langle f\rangle = f(\theta) + \sum_{n=1}^{\infty}\left(\frac{Q_\infty\varepsilon}{4}\right)^n \mathcal{F}^{(n)}\{f(\theta)\}. \tag{13b}$$

As expected, in the limit $\varepsilon \to 0$ (i.e., $s^* \to \infty$), (13) degenerates into the classic (rigid case) solution. Additionally, the actuation term appears with the coefficient ε, namely, spatial actuation does not affect the leading order but higher orders.

Table 1 presents numerical validation results for (13), achieved by COMSOL Multiphysics®. The numerical model used is described in Appendix B. To demonstrate the influence of chord-wise elasticity on the twist angle, we focus on the ratio between the (dimensional) twisting angle δ in the elastic case to the rigid case, denoted hereafter R_δ. To isolate elasticity

Table 1

Heatmap of the model accuracy in predicting the elasticity influence on the rotation angle. The ratio between the twisting angle δ in elastic case and δ in rigid case represents the elasticity influence on the twist angle. The values in the table were obtained by dividing this ratio's analytic value by the ratio's numeric value for each combination of initial angle-of-attack and torsional spring stiffness, see (14). The mean absolute error is 1.6%.

α_0 [°]	5000	5500	6000	6500	7000	7500	8000
0.5	100.98%	100.85%	100.90%	100.87%	100.85%	100.84%	100.80%
1	101.23%	101.01%	100.88%	100.83%	100.82%	100.79%	100.79%
1.5	101.61%	101.24%	101.04%	100.96%	100.88%	100.80%	100.77%
2	101.96%	101.49%	101.25%	101.08%	100.99%	100.88%	100.87%
2.5	102.49%	101.75%	101.43%	101.22%	101.10%	101.02%	100.95%
3	102.85%	102.11%	101.65%	101.40%	101.24%	101.11%	101.04%
3.5	103.76%	102.46%	101.86%	101.56%	101.34%	101.24%	101.14%
4	104.73%	103.12%	102.31%	101.95%	101.69%	101.50%	101.34%
4.5	106.55%	104.04%	102.93%	102.24%	101.83%	101.59%	101.41%

Initial angle-of-attack, α_0 [°]

Torsional spring stiffness, k [N · m/rad]

influence, regardless of the calculation method, we take the analytic results for R_δ, and divide them by the corresponding COMSOL results for R_δ, reads

$$\frac{R_{\delta,\text{model}}}{R_{\delta,\text{COMSOL}}} = \frac{\left(\delta_{\text{elastic}}/\delta_{\text{rigid}}\right)_{\text{model}}}{\left(\delta_{\text{elastic}}/\delta_{\text{rigid}}\right)_{\text{COMSOL}}}. \tag{14}$$

The results are presented as a heatmap in Table 1 for $0.5\,[°] \leq \alpha_0 \leq 4.5\,[°]$ and $5\,[\text{kN m/rad}] \leq k \leq 8\,[\text{kN m/rad}]$. The mean absolute error is 1.6%, and the maximal absolute error is 6.5% (for the extreme combination of $\alpha_0 = 4.5\,[°]$ and $k = 5\,[\text{kN m/rad}]$, were nonlinear effects increase, see Appendix B). The results show that our model nicely captures the elasticity influence on the rotation angle.

3.3. Static instability - divergence

In a similar manner to classic static aeroelasticity, the divergence dynamic pressure is obtained when the denominator of the solution for Δ vanishes (Dowell et al., 2005). We begin with the leading-order solution for the elastic equation, (11). Taking the denominator in (13) and rearranging it, we obtain a quadratic equation for divergence dynamic pressure ratio, elastic to rigid,

$$\frac{\mathcal{M}_{X_{EA}}\langle \mathcal{A}(\theta)\rangle}{\left[2\pi\left(X_{EA} - \frac{1}{4}\right)\right]^2}\frac{K\varepsilon}{4}\left(\frac{Q_{\infty,d}}{Q_{\infty,d,r}}\right)^2 + \frac{Q_{\infty,d}}{Q_{\infty,d,r}} - 1 = 0, \tag{15}$$

where $Q_{\infty,d,r} = K/2\pi\left(X_{EA} - \frac{1}{4}\right)$ is the normalized divergence dynamic pressure for the rigid case [which is readily obtained from the denominator in (13) while taking the limit $\varepsilon \to 0$], and $\varepsilon K/4 = kc/s^*$ is a dimensionless ratio of the torsional spring stiffness and elastic stiffness. This ratio multiplies a term depending only on X_{EA}, so that the solution depends solely on two dimensionless parameters. The (single) positive root for each combination of these parameters (where $\mathcal{M}_{X_{EA}}\langle \mathcal{A}(\theta)\rangle$ was calculated for NACA 4-digit airfoil thickness distribution) is shown in the contour map presented in Fig. 2 for the range $1/4 \leq X_{EA} < 1$, the validity range of $Q_{\infty,d,r}$. For the limit $s^* \to \infty$, the elasticity influence is negligible, thus the ratio $Q_{\infty,d}/Q_{\infty,d,r}$ approaches 100%, as expected. Likewise, for $X_{EA} \to 1/4$ the ratio $Q_{\infty,d}/Q_{\infty,d,r}$ approaches 0 since $Q_{\infty,d,r}$ approaches infinity. However, the entire map presents values smaller than 100%, which means that the elasticity increases the divergence onset. For each value of kc/s^*, the highest ratio is obtained at $X_{EA} \approx 0.44$. There, the effect of elasticity on the divergence onset is the smallest; the divergence condition is the closest to the rigid case with the same torsional spring stiffness. There is no actuation term in (15); a distributed actuation cannot delay or cancel divergence only by applying a direct moment.
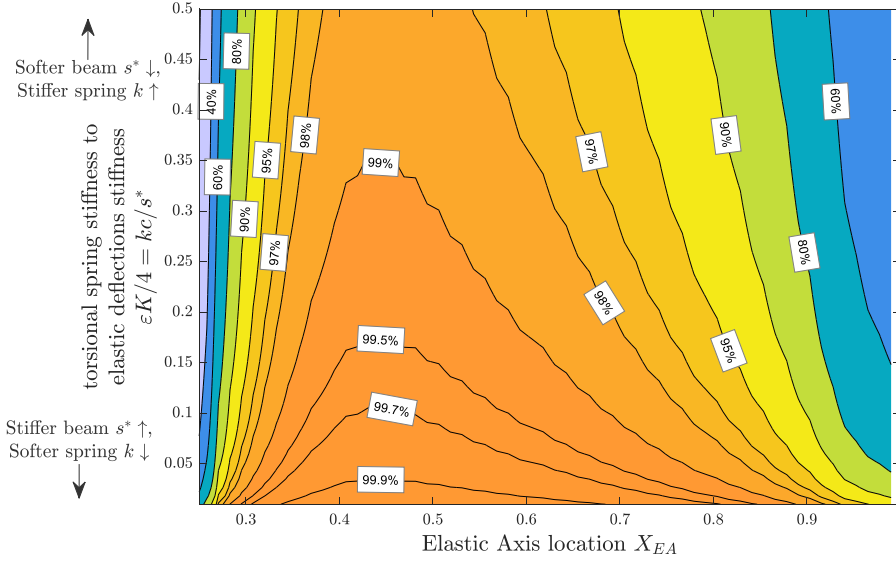
Fig. 2. Contour map of the divergence dynamic pressure ratio (elastic to rigid), $\mathbf{Q_{\infty,d}/Q_{\infty,d,r}}$. The results are presented as the function of the elastic axis location and the ratio of the torsional spring stiffness and elastic stiffness. The results are presented for $X_{EA} > 1/4$, the rigid case range of validity. The ratio approaches 100% for negligible elasticity and zero at quarter-chord since the divergence dynamic pressure for the rigid case is infinite. The effect of elasticity on the divergence onset is the smallest at $X_{EA} \approx 0.44$.

We extend the results for $X_{EA} < 1/4$ by rearranging the denominator in (13) into

$$\frac{\varepsilon K}{4} \mathcal{M}_{X_{EA}} \langle \mathcal{A}(\theta) \rangle \left(\frac{Q_\infty}{K} \right)^2 + 2\pi \left(X_c - \frac{1}{4} \right) \frac{Q_\infty}{K} - 1 = 0. \tag{16}$$

The log of the (sole) positive root of $Q_\infty/K = q_\infty c^2/k$ for each combination of the abovementioned parameters is shown in Fig. 3 [dimensional solution for the divergence airspeed is given in Eq. (A.5)]. As can be seen, for $X_{EA} < 1/4$ there are much higher values than for $X_{EA} > 1/4$, i.e., the aerodynamic moment is much higher than torsional stiffness. The classic (rigid) aeroelasticity theory states that divergence cannot occur if the elastic axis is at the front quarter-chord. However, for sufficiently chord-wise elasticity, there exists a physical solution for divergence even $X_{EA} < 1/4$, i.e., the denominator in the solution for Δ vanishes.

Next, we examine the leading- and first-order solution. Taking the denominator and rearranging it as for (15), we obtain a cubic equation for divergence dynamic pressure ratio, elastic to rigid,

$$\left(\frac{K\varepsilon}{4} \right)^2 \frac{\mathcal{M}_{X_{EA}} \langle \mathcal{F}\{\mathcal{A}(\theta)\} \rangle}{[2\pi (X_{EA} - \frac{1}{4})]^3} \left(\frac{Q_\infty}{Q_{\infty,d,r}} \right)^3 + \frac{\mathcal{M}_{X_{EA}} \langle \mathcal{A}(\theta) \rangle}{[2\pi (X_{EA} - \frac{1}{4})]^2} \frac{K\varepsilon}{4} \left(\frac{Q_\infty}{Q_{\infty,d,r}} \right)^2 + \frac{Q_\infty}{Q_{\infty,d,r}} - 1 = 0. \tag{17}$$

However, the results obtained are very close to those of the leading-order, given in Fig. 2; the additional order contribution is less than 1%. Nevertheless, one may observe that the camber contribution does not appear in (13)'s denominator; the airfoil shape affects implicitly via the spatial deflection stiffness, $S(X)$ (see explicit expressions in Appendix A). For comparison, Appendix C contains graphical results calculated for uniform spatial stiffness (i.e., $S \equiv 1$). See Fig. 7.

3.4. Influence on aerodynamic properties

In this section, we examine the role of chord-wise elasticity on lift and pitching moment. For that aim, we substitute the approximations for the elastic deflection and twist angle, (12) & (13), into (3b), yielding the aerodynamic distributed load for an elastic airfoil. The solutions obtained are governed explicitly by the dimensionless ratio between aerodynamic moment and bending stiffness, $Q_\infty \varepsilon/4$, and implicitly by X_{EA} and S [via $\mathcal{A}$ and $\mathcal{F}$, see (A.1) to (A.3)]. The results are presented as a function of these parameters, where we calculated $\mathcal{A}$ and $\mathcal{F}$ for NACA 4-digits airfoil thickness distribution.

Integrating the aerodynamic load over the airfoil yields the lift coefficient

$$c_l = 2\pi \alpha + 2 \int_0^\pi \left(\frac{dw_0}{dx} + \frac{d\tilde{d}}{dx} \right)_\phi [\cos(\phi) - 1] \, d\phi. \tag{18}$$
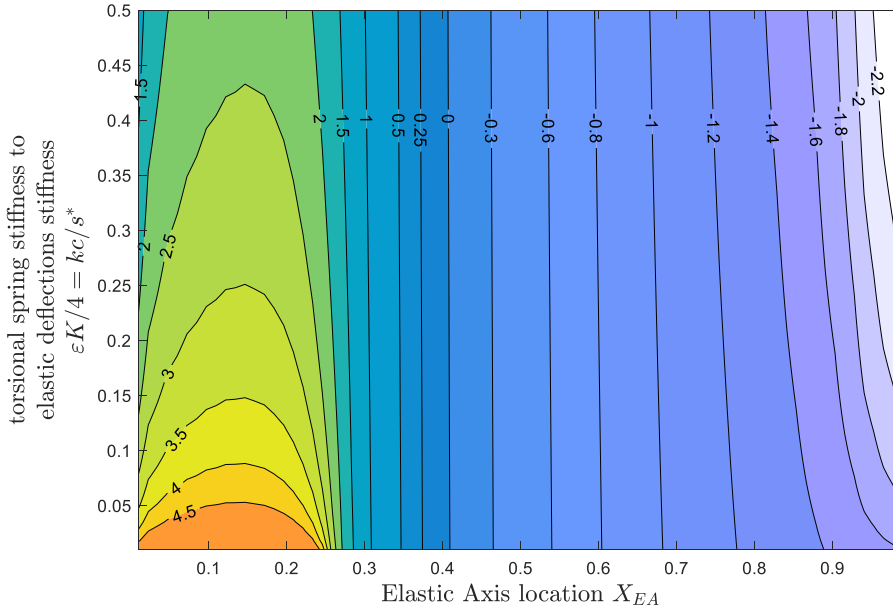
Fig. 3. Normalized divergence dynamic pressure to normalized rotational spring stiffness, $\ln\left(Q_{\infty,d}/K\right)$. The ratio $Q_{\infty,d}/K$ is equivalent to dimensional divergence dynamic pressure, normalized by k/c^2. The significance and innovation of the results are that there exists a physical solution for divergence, even for $X_{EA} < 1/4$, unlike the rigid case. The physical condition for this is that the aerodynamic moment is much higher than the torsional stiffness.

The aerodynamic load is determined by both angle-of-attack and camber slope, as (18) indicates. Using (12) & (13), one may examine the influence on the lift of each problem parameter. However, the initial camber has a constant contribution, while the angle-of-attack usually changes during flights. Hence, a more meaningful property is the lift curve slope, $c_{l,\alpha}$. Differentiating (18) w.r.t. α gives

$$c_{l,\alpha} = 2\pi + 2\frac{Q_\infty \varepsilon}{4}\left\{\int_0^\pi \mathcal{S}\langle\mathcal{A}\rangle\left[\cos(\phi) - 1\right]\mathrm{d}\phi\right\}. \tag{19}$$

To examine whether exists an aerodynamic center (viz., location for which the pitch moment is independent of angle-of-attack), we write the moment term for an unknown aerodynamic center location, x_{AC}, then take the derivative w.r.t. α and compel it to be zero:

$$\frac{\partial M_{AC}}{\partial \alpha} = \frac{\partial}{\partial \alpha}\int_0^c \Delta p\,(x - x_{AC})\,\mathrm{d}x = 0. \tag{20}$$

Using the relation $\cos(\theta_{AC}) = 1 - 2X_{AC}$, we obtain the aerodynamic center as

$$X_{AC} = \frac{\frac{\pi}{2} - \frac{Q_\infty \varepsilon}{4}\int_0^\pi \mathcal{S}\langle\mathcal{A}\rangle\left[1 - \cos(\phi) - \sin^2(\phi)\right]d\phi}{2\pi - \frac{Q_\infty \varepsilon}{2}\int_0^\pi \mathcal{S}\langle\mathcal{A}\rangle\left[1 - \cos(\phi)\right]d\phi}. \tag{21}$$

As expected, the solutions degenerate into the classic solutions for rigid cases, i.e., $c_{l,\alpha} \xrightarrow{\varepsilon \to 0} 2\pi$ and $X_{AC} \xrightarrow{\varepsilon \to 0} 1/4$.

Fig. 4 serves graphical results of (19) and (21), calculated for NACA 4-digits airfoil thickness distribution. For convenience, the results are normalized by the rigid cases' values. Fig. 4a shows that the elastic axis location in the fore half chord slightly decreases the lift line slope. However, for $X_{EA} > 0.53$ chord-wise elasticity increases the lift curve slope. Fig. 4b shows that chord-wise elasticity brings the aerodynamic center slightly forward, as in cambered airfoils. Those effects surge for $X_{EA} > 0.85$. For comparison, see corresponding results, calculated for uniform stiffness (Fig. 8 in Appendix C).

3.5. The use of actuation in the limit of negligible airfoil twist

In this section, we present some practical applications of *actuated* shape-morphing airfoils. For simplicity, we take the limit where $k \to \infty$, (3c) compels $\delta \to 0$, hence $\alpha \equiv \alpha_0$, $d \equiv \tilde{d}$; This limit is equivalent to replacing the spring with a fixture, and (6b) is no longer valid.

Each of the results presented in this section is accompanied by an illustrating case, solved by numerical simulation. The specific method in which actuation is achieved is not essential to the analysis, and here we arbitrarily chose camber actuation by a distribution of pressurized internal chambers, commonly used in the field of soft robotics. Such an
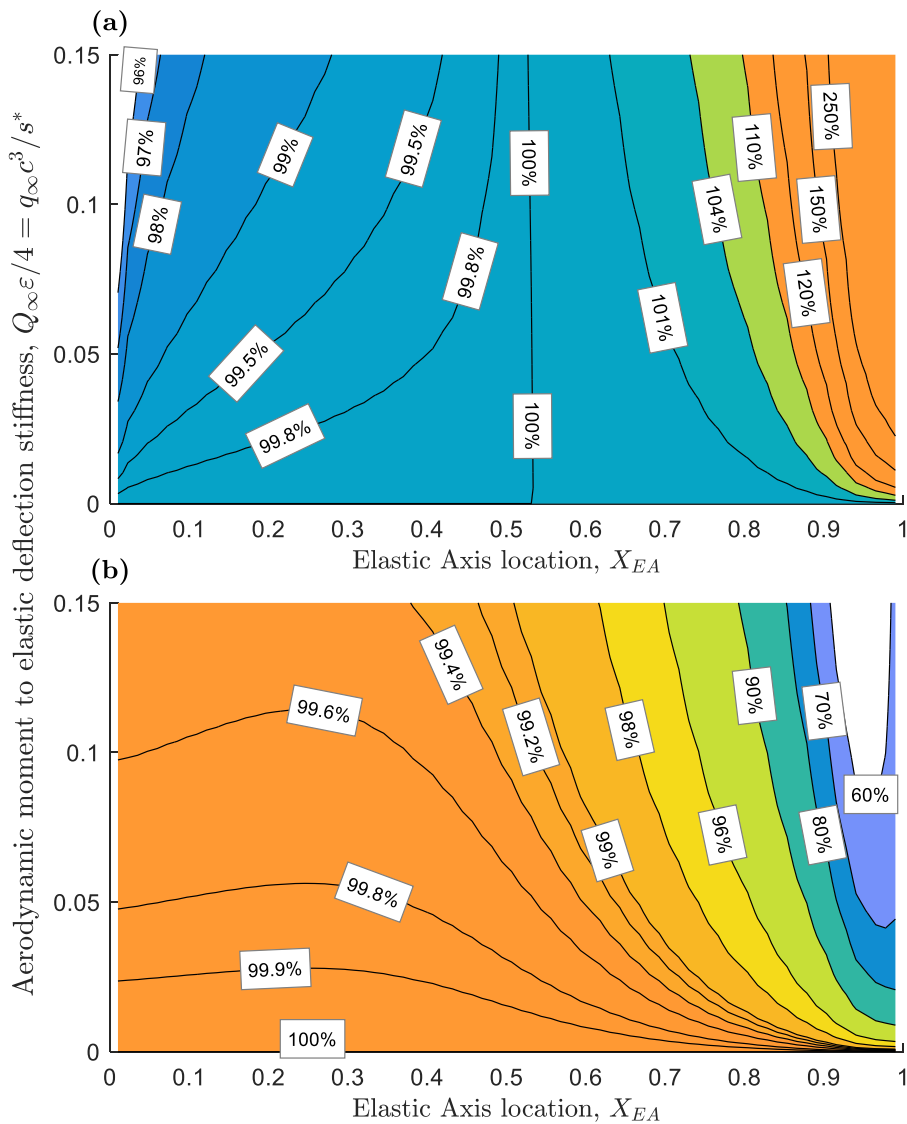
Fig. 4. Influence on aerodynamic properties. The results are presented as the function of the elastic axis location and the ratio between aerodynamic moment and bending stiffness, calculated for NACA 4-digits airfoil thickness distribution. Panel (a) presents the lift curve slope deviation from 2π, $c_{l,\alpha}/2\pi$. The slope increases as X_{EA} moves backward and exceeds 2π at $X_{EA} \approx 0.53$. Panel (b) presents the aerodynamic center location deviation from the quarter chord, $x_{EA}/(c/4)$. The values are smaller than 100%, i.e., chord-wise elasticity brings the aerodynamic center forward.

actuation approach is known as embedded-fluidic-networks or pneumatic-artificial-muscles (Thill et al., 2008). Results and discussions are presented below. Details concerned with the numerical model, physical and geometric parameters, and the actuation method can be found in Appendix D.

An explicit expression for the steady deflection of a uniformly actuated airfoil was obtained using (11) and (12), with additional integration and application of the clamping boundary conditions (7a). Results for the steady deflection of a uniformly actuated airfoil are presented in Fig. 5a, which compares the difference between the numerical calculation w_n and the analytic results w_a. The channel distribution is presented at the insert. Difference between the results is presented for no-correction (smooth line), leading-order correction (dashed line), and first-order correction (dotted line). The asymptotic scheme clearly reduces the discrepancy between the analysis and the numerical computation by increasing the order of the correction terms.

For known fluid and airfoil properties, a non-uniformly distributed actuation can be applied to achieve reduced aeroelastic deflection of soft airfoils or to create a transition between two predefined cambers. By setting the deformation D and solving for the actuation D_a, it is possible to solve (6a) without applying the asymptotic expansion (8).
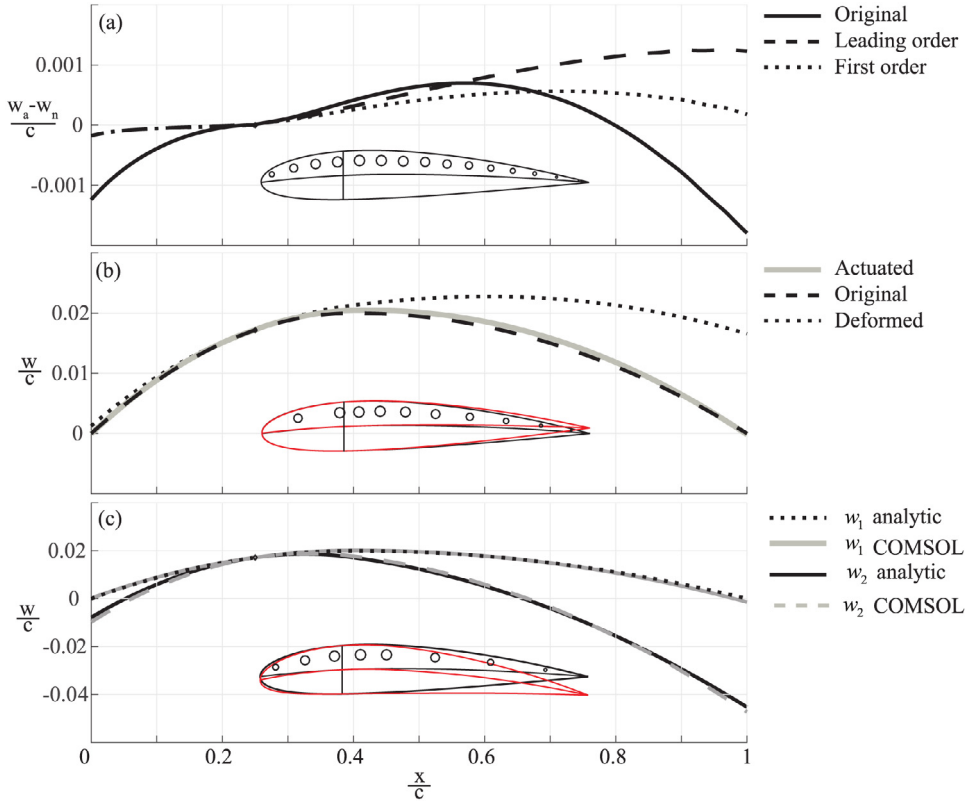
Fig. 5. Illustrative examples for actuation. Small inserts depict the shape of the airfoil and the layout of an embedded-fluidic-network actuation mechanism spaced along its chord (see circles), as presented in Appendix D. Panel (a) presents results for the asymptotic expansion in the form of the spatial error of the leading and first orders compared with the numerical solution (w_a denotes the analytic solution, w_n the numerical calculation), the actuation network is spaced uniformly along the chord. Panel (b) presents the case of cancellation of aeroelastic deformation using embedded actuation. The dotted line and red airfoil insert show the steady-state, unactuated, aeroelastic deflection. The actuated camber (solid line) is based on a channel layout designed to deform the airfoil into its original form (dashed line). Good agreement is achieved in this case between the original and actuated airfoil shapes. Panel (c) presents the results of applying embedded actuation to transform a NACA-2412 airfoil into a NACA-4412 airfoil (modification of camber). Good agreement in airfoil shape is shown between the analytic and numerical solutions (destination airfoil shown in red insert).

Cancellation of steady aeroelastic deflection by distributed actuation is immediately calculated from (6a) by setting $D = 0$, yielding dD_a/dX by

$$\frac{dD_a}{dX} = -\frac{Q_\infty}{4}(\tilde{\alpha}_0 + \Delta)\mathcal{A}(\theta) - \frac{Q_\infty}{4}\Pi\mathcal{F}\left\{\frac{dW_0}{dX}\right\}(\theta), \tag{22}$$

and the additional integration coefficient is obtained from clamping boundary conditions (7a). Fig. 5b presents deformation cancellation, which determines the required actuation, and, thus, the geometry of the chambers (see insert). The camber at rest is marked by a dashed line, and the deformed, unactuated camber is denoted by a dotted line. The numerical calculation for a camber actuated according to (22) is marked by a smooth line. Explicit agreement between the numerical calculation and the analytic results is evident.

Similarly, a transition between two predefined cambers $W_1(X)$ and $W_2(X)$ can be readily obtained by the following scheme:

(I) setting $D_a = 0$ and $W_0 = W_1 - D\varepsilon/\Pi$ in (6a) and solving for D. In this case the RHS integral in (6a) contains only W_1. Hence, the equation is no longer an integrodifferential equation, and D can be calculated by integration. From D the initial camber at rest W_0 is obtained for which the profile W_1 is achieved for $D_a = 0$.

(II) After calculating W_0, D_a can be calculated by setting $D\Pi/\varepsilon = W_2 - W_0$ into (6a) and solving for D_a yielding camber W_2.

Fig. 5c presents comparisons for the transformation of NACA-2412 camber to NACA-4412 camber. Good agreement between the analysis and numerical computations is also presented for this case.

4. Concluding remarks

Recent research deals with chord-wise aeroelasticity in the context of morphing wing sections due to their potential to enhance the performance of aircraft structures. However, numerical and experimental studies mostly examine a specific configuration, whereas general theoretic analyses of airfoils are rare. In this work, we model a general airfoil as two cantilever beams connected to a torsional spring at an arbitrary location amid its camber. This structure is subjected to distributed aerodynamic load given by the thin airfoil theory; thus, we obtained an integrodifferential equation governing the elastic deflection. We expanded the elastic deflection asymptotically and obtained an approximated solution, allowing us to examine the influence of chord-wise elasticity on the aerodynamic properties.

Moreover, our model includes a general actuation term; thus, it lays a theoretical foundation for an ideal design of shape-morphing soft airfoils. To validate these results, we compared our solutions with numerical simulations utilizing a commercially available code. Good agreements were achieved in all cases examined, including the application of embedded actuation to modify an airfoil camber, thus affecting its aerodynamic properties. Next, we obtained the airfoil rotation angle via the moment balance between the aerodynamic load and torsional spring. The corresponding numerical validation shows that our model nicely captures the elasticity influence on the rotation. In addition, we obtained the divergence dynamic pressure by examining whether the denominator of the solution for the twist angle vanishes. The results contour maps show that introducing chord-wise elasticity enhances divergence onset. Furthermore, unlike the rigid case, there exists a physical solution for divergence for the front quarter-chord. It should be noted that it is the only static instability mode discussed; Other kinds of static instabilities arising due to the introduction of chord-wise elasticity (such as buckling) may also exist, but are not considered instabilities in the model [although others may consider any nonoscillatory static instability as divergence (e.g., Païdoussis et al., 2010)].

A limiting simplifying assumption used in the current study was calculating the aerodynamic load of deformed configurations via thin wing theory, although their chord does not coalesce with the abscissa. This gap might be surmounted by transforming the deviation into an effective additional angle-of-attack and using a translated configuration in the calculations. However, as the numerical validations present, the results give an excellent approximation for the majority of our analysis domain. In addition, the Euler–Bernoulli equation is applicable only for slender beams; hence, the results are not valid near $X_{EA} = 0$ or $X_{EA} = 1$. Nevertheless, the elastic axis location is far from the edges under most circumstances.

Declaration of competing interest

The authors declare that they have no known competing financial interests or personal relationships that could have appeared to influence the work reported in this paper.

Data availability

Data will be made available on request

Appendix A. Complementary expressions

Integrating (9a) twice and applying boundary conditions (7b), yields:

$$\frac{4S}{Q_\infty} \frac{\mathrm{d}^2 (D_0 - D_a)}{\mathrm{d}X^2} = (\tilde{\alpha}_0 + \Delta)\, a(\theta) + \Pi f \left\langle \frac{\mathrm{d}W_0}{\mathrm{d}X} \right\rangle \tag{A.1}$$

where

$$a(\theta) = \frac{\theta}{2} + \sin(\theta) - \frac{\sin(2\theta)}{4} - \theta \cos(\theta) + \pi \left(\frac{1}{2} - 2X\right) H(X - X_{ea}), \tag{A.2}$$

and

$$f\left\langle \frac{\mathrm{d}W_0}{\mathrm{d}X} \right\rangle = \int_0^\pi \left(\frac{\mathrm{d}W_0}{\mathrm{d}X}\right)_\phi \left\{ \left[\cos(\theta)\cos(\phi) - \frac{\cos(2\phi)}{2}\right] H(X - X_{ea}) - \frac{a(\theta)}{\pi} \right\} \mathrm{d}\phi$$
$$+ \frac{2}{\pi} \sum_{n=1}^\infty \int_0^\pi \frac{\mathrm{d}w}{\mathrm{d}x} \cos(n\varphi)\, \mathrm{d}\varphi \lim_{k \to n} \frac{\sin(k\theta)\left[(k^2 + 2)\cos(2\theta) - k^2 + 4\right] - 3k \sin(2\theta)\cos(k\theta)}{(k^2 - 4)(k^2 - 1)} \tag{A.3}$$

We denoted H for the Heaviside theta function. The solution for spatial slope (11) (as well as elastic deflection) is readily obtained by integrating (A.1) and applying (7a). Thus, (11) depends on both the spatial stiffness $S(X)$ and the elastic axis location X_{EA}.

Solving (16) for the divergence dynamic pressure, the positive root is

$$Q_{\infty,d} = 4\pi \left(X_{EA} - \frac{1}{4}\right) \frac{\sqrt{1 + \frac{\varepsilon K \cdot \mathcal{M}_{X_{EA}} \langle \mathcal{A}(\theta) \rangle}{4\pi \left(X_{EA} - \frac{1}{4}\right)}} - 1}{\varepsilon \mathcal{M}_{X_{EA}} \langle \mathcal{A}(\theta) \rangle}, \tag{A.4}$$
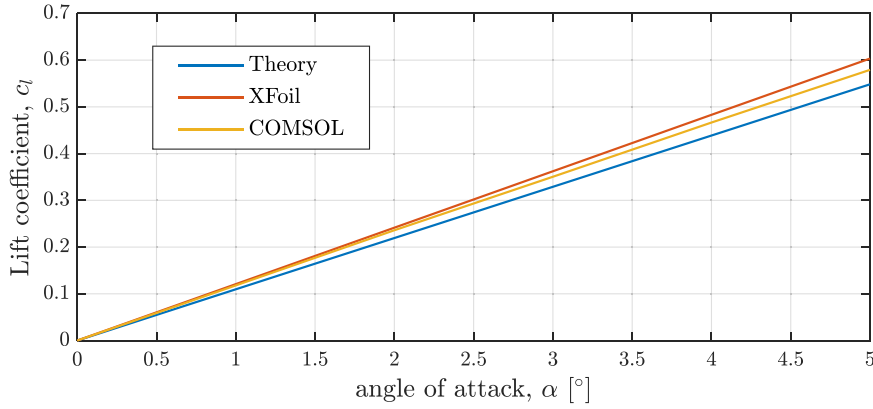
Fig. 6. Comparison of lift coefficient vs. angle of attack for rigid NACA-0012 airfoil. The lift coefficient was calculated using XFoil and COMSOL and compared with the thin wing theory result - $c_{l,\alpha} = 2\pi$. XFoil results show $c_{l,\alpha} \approx 2.2\pi$ while COMSOL results show $c_{l,\alpha} \approx 2.12\pi$.

or, solving for the dimensional airspeed,

$$u_{\infty,d} = \sqrt{2s^* \pi \left(X_{EA} - \frac{1}{4} \right) \frac{\sqrt{1 + \frac{kc \cdot \mathcal{M}_{X_{EA}} \langle \mathcal{A}(\theta) \rangle}{s^* \pi \left(X_{EA} - \frac{1}{4} \right)}} - 1}{\rho_\infty c^3 \cdot \mathcal{M}_{X_{EA}} \langle \mathcal{A}(\theta) \rangle}}. \tag{A.5}$$

Eq. (16) contains only the leading-order approximation. For any higher-order, one needs to solve a polynomial of degree that corresponds to the asymptotic expansion used.

Appendix B. The numerical model used in Section 3.2

For the development of the thin airfoil theory, it is assumed that maximum airfoil thickness is small compared to chord length, and that camberline shape deviates only slightly from the chord line. Therefore, the vorticity is distributed on the chordline, whereas the non-penetration condition is satisfied on the camberline. Hence, to minimize the deviation between theory and numerical simulation, we focus on a symmetric NACA-0012 airfoil geometry: its camberline coalesces with its chordline.

First, we examined a rigid, non-rotating configuration. We calculated the lift coefficient at various angles-of-attack using XFoil™ (inviscid formulation, linear-vorticity stream function panel method) and compared it to the theoretical results, as Fig. 6 presents. In addition, we calculated lift utilizing COMSOL Multiphysics'® Fluid–Structure Interaction (FSI) module, i.e., Navier–Stokes equations and Cauchy equation. The airfoil chord was $c = 1$ [m], fluid density was $\rho_\infty = 1.006 \left[\text{kg/m}^3 \right]$ (taken from standard atmosphere model for an altitude of 2 [km]), and the uniform potential flow velocity was $u_\infty = 40$ [m/s]. To easily introduce elasticity in later steps, we used the Fluid-Solid-Interaction module with an airfoil's Young modulus $E = 70$ [GPa] (aluminum). The grid consisted of 7×10^3 first-order unstructured quad elements with an average (skewness-based) element quality of 0.89 for the fluidic domain and 10^3 second-order unstructured triangular elements with average element quality of 0.85 for the solid domain. The size of the rectangular domain was $6c \times 10c$, rotated by α_0 so that the velocity condition at the front boundary is perpendicular to the boundary. The model included 4×10^4 degrees of freedom. All our solutions converged by at least four orders of magnitude from the value given at the initial condition.

Fig. 6 compares the lift coefficients calculated numerically with the theoretical values. We found that COMSOL's result for lift curve slope is closer to the theoretical result of $c_{l,\alpha} = 2\pi$ than XFoil's (error of 5.8% vs. 10%). Henceforth, a 6% error is considered acceptable.

Thus, we proceeded to the next step and examined a rigid rotatable configuration with an elastic axis at $X_{EA} = 0.75$. To facilitate significant rotation angles, we partitioned the fluid domain by a circle with a radius of $1.5c$, so that its interior mesh was allowed to deform and its border allowed to slip relative to the outer meshed domain. Nevertheless, since the resulting rotation angles' values were small, the results are presented in Table 2 as the ratio of (dimensional) δ given by the classic quasisteady aeroelasticity theory to COMSOL's result for the angle of rotation δ. The mean absolute deviation for $0 < \alpha_0 \leq 4.5$ [°] and 5 [kN m/rad] $\leq k \leq 8$ [kNm/rad] was 5%, and maximal absolute deviation of 20% (for the extreme combination of $\alpha_0 = 4.5$ [°] and $k = 5$ [kN m/rad], were nonlinear effects increase).

Eventually, we enhanced the airfoil elasticity by using Young's modulus $E = 300$ [MPa] so that, by (6d), $\varepsilon \approx 0.3$. Since we deal with a non-actuated symmetric configuration, R_δ is independent of the initial angle-of-attack, as can be seen by

Table 2
Ratios of δ values (classic aeroelasticity theory to COMSOL) for a rigid rotatable airfoil. The results were calculated for a NACA-0012 airfoil with $X_{EA} = 0.75$, $\alpha_0 = 4.5$ [°] and k = 5 [kN m/rad], were nonlinear effects increase. This table aims to validate the numerical computation for rigid airfoils prior to comparison with our model for elastic airfoils.

Initial angle-of-attack, α_0 [°]	5000	5500	6000	6500	7000	7500	8000
0.5	90.91%	92.00%	92.62%	93.13%	93.50%	93.79%	94.06%
1	90.41%	91.38%	92.09%	92.59%	92.94%	93.24%	93.47%
1.5	93.10%	93.36%	93.69%	93.97%	94.23%	94.47%	94.65%
2	94.92%	94.35%	94.24%	94.28%	94.38%	94.51%	94.58%
2.5	96.77%	95.43%	94.91%	94.70%	94.63%	94.62%	94.66%
3	100.83%	98.32%	97.19%	96.57%	96.23%	96.04%	95.92%
3.5	105.51%	101.38%	99.42%	98.34%	97.71%	97.28%	97.02%
4	110.19%	104.02%	101.14%	99.56%	98.61%	98.00%	97.62%
4.5	119.53%	110.30%	105.66%	103.12%	101.60%	100.59%	99.89%

Torsional spring stiffness, k [N· m/rad]

Table 3
Ratios between δ values, elastic to rigid. (a) values obtained by COMSOL simulations. (b) values obtained by the model, (B.1). The numerical results present dependence on the initial angle-of-attack but not the model. For relatively small values of δ (for small k and α_0), the deviation is stronger than for large values of δ. As the torsional stiffness increases, the ratio values converge to an approximated value of 103%.

(a)

Initial angle-of-attack, α_0 [°]	5000	5500	6000	6500	7000	7500	8000
4.5	100.15%	101.73%	102.27%	102.57%	102.68%	102.70%	102.71%
4	101.90%	102.63%	102.90%	102.86%	102.83%	102.79%	102.78%
3.5	102.85%	103.30%	103.34%	103.26%	103.18%	103.06%	102.98%
3	103.76%	103.66%	103.56%	103.42%	103.28%	103.18%	103.08%
2.5	104.12%	104.02%	103.78%	103.60%	103.43%	103.28%	103.17%
2	104.66%	104.29%	103.97%	103.75%	103.55%	103.42%	103.25%
1.5	105.03%	104.55%	104.18%	103.87%	103.65%	103.50%	103.35%
1	105.42%	104.78%	104.35%	104.01%	103.72%	103.51%	103.33%
0.5	105.68%	104.95%	104.33%	103.96%	103.68%	103.46%	103.32%

(b)

5000	5500	6000	6500	7000	7500	8000
106.72%	105.84%	105.27%	104.87%	104.57%	104.33%	104.15%

Torsional spring stiffness, k [N· m/rad]

substituting $\Pi W_0 = D_a = 0$:

$$R_{\delta,sym} = \frac{\frac{2\pi\left(X_{EA}-\frac{1}{4}\right)+\varepsilon\frac{Q_\infty}{4}\,\mathcal{M}_{X_{EA}}\langle\mathcal{S}\langle\mathcal{A}\rangle\rangle}{K/Q_\infty-2\pi\left(X_{EA}-\frac{1}{4}\right)-\varepsilon\frac{Q_\infty}{4}\,\mathcal{M}_{X_{EA}}\langle\mathcal{S}\langle\mathcal{A}\rangle\rangle}\tilde{\alpha}_0}{\frac{2\pi\left(X_{EA}-\frac{1}{4}\right)}{K/Q_\infty-2\pi\left(X_{EA}-\frac{1}{4}\right)}\tilde{\alpha}_0}$$

(B.1)

The results obtained by COMSOL, however, present dependence on the initial angle-of-attack, α_0, as Table 3 shows. Generally, R_δ is larger than for small values of α_0 than for relatively large values of α_0, and it is so for k values as well. It is noted that the absolute values of the rotation angles are small. For instance, the combination of $k = 5$ [kN m/rad] and $\alpha_0 = 0.5$ [°] gave $\delta_{soft} \approx 0.9$ [°] versus $\delta_{rigid} \approx 0.85$ [°]. This fact is an outcome of the asymptotic approximation
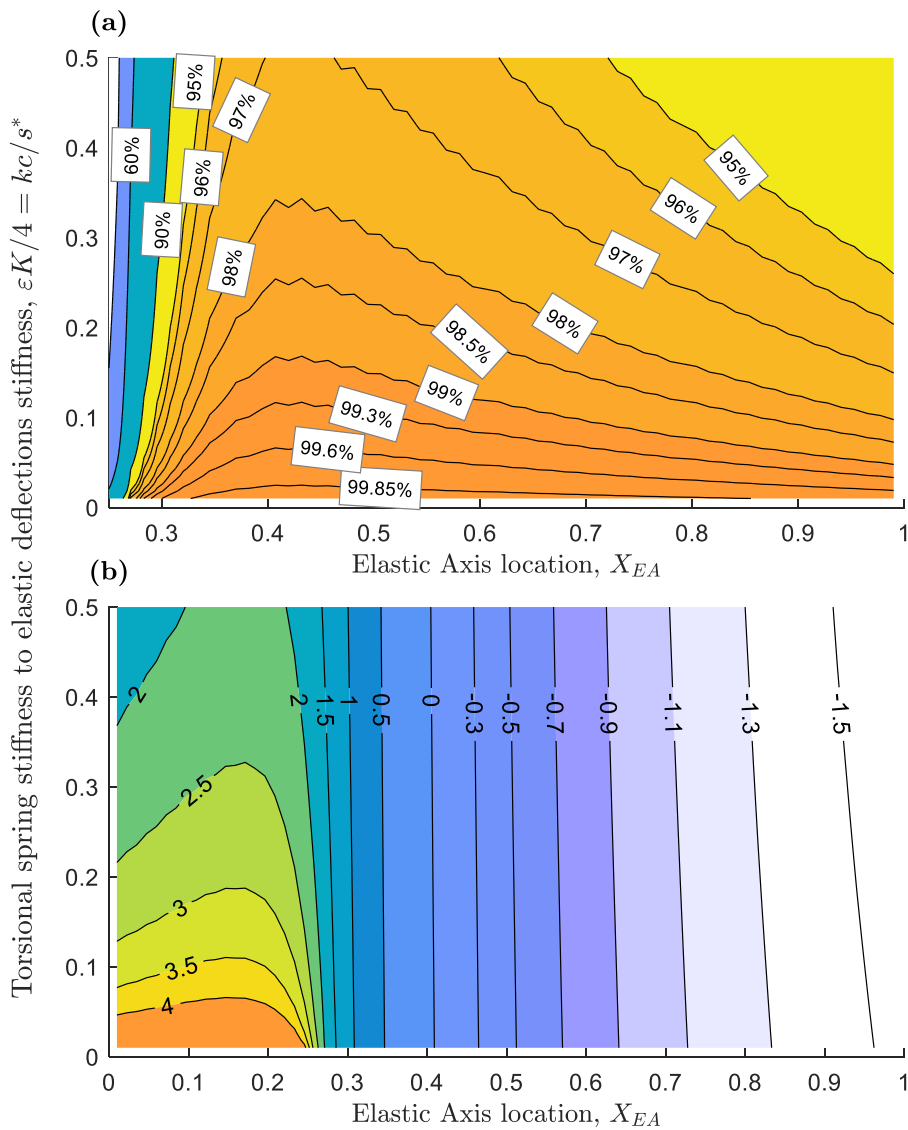
Fig. 7. Divergence dynamic pressure for uniform stiffness. Panel (a) corresponds to Fig. 2 and presents the divergence dynamic pressure ratio (elastic to rigid), $Q_{\infty,d}/Q_{\infty,d,r}$. For uniform spatial stiffness, the ratio depends on kc/s^* rather than on X_{EA}, compared to Fig. 2. Panel (b) corresponds to Fig. 3 and presents normalized divergence dynamic pressure to normalized rotational spring stiffness, $\ln\left(Q_{\infty,d}/K\right)$. The values obtained are smaller than Fig. 3.

for relatively small ε. Nonetheless, by examining the ratios $R_{\delta,\mathrm{model}}/R_{\delta,\mathrm{COMSOL}}$ presented in Table 3, we conclude that our model, although approximated, well captures the elasticity influence on the rotation angle.

Appendix C. Results for uniform stiffness

The results presented in Sections 3.2 and 3.4 were calculated using the spatial bending stiffness of NACA 4-digits airfoil thickness distribution based on its local thickness. However, the stiffness of an actual airfoil is determined by its internal structure, such as reinforcing ribs, stiffened tips, etc. Thus, for comparison, we add here results while using uniform spatial stiffness (i.e., $S \equiv 1$) in the calculations of $\mathcal{A}$ and $\mathcal{F}$.

Fig. 7 presents the divergence dynamic pressure ratio, discussed in Section 3.2, for uniform airfoil stiffness. Panel (a) presents the ratio $Q_{\infty,d}/Q_{\infty,d,r}$ [solution of (15)]. For uniform spatial stiffness, the ratio depends on kc/s^* rather than on X_{EA}, compared to the results in Fig. 2. Panel (b) presents the natural logarithm of $Q_{\infty,d}/K$ [solution of (16)]. The obtained values are smaller than those in Fig. 3.

Fig. 8 corresponds to Fig. 4, which presents the influence on aerodynamic properties, discussed in Section 3.3, for uniform airfoil stiffness. Panel (a) presents the lift curve slope deviation from 2π, $c_{l,\alpha}/2\pi$. Like Fig. 4, the slope increases
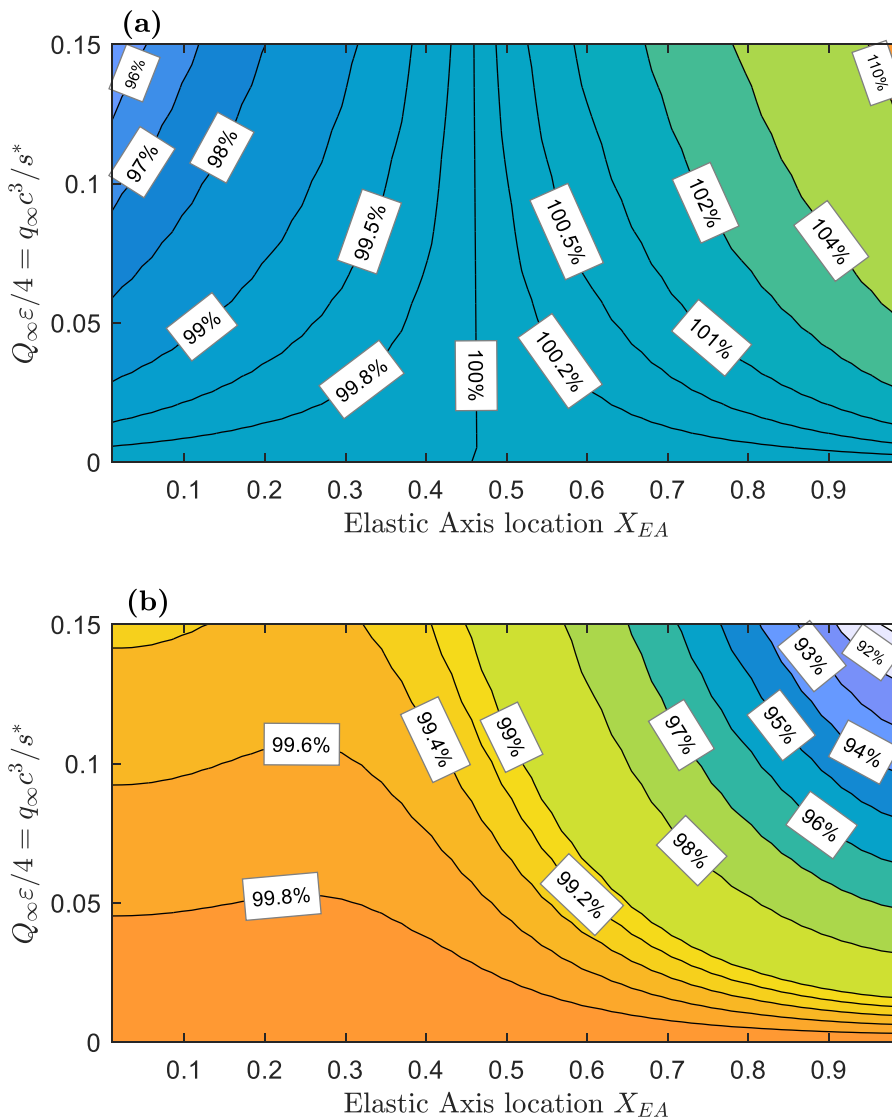
Fig. 8. Influence on aerodynamic properties for uniform stiffness. The results are presented as the function of the elastic axis location and the ratio between aerodynamic moment and bending stiffness, calculated for uniform spatial stiffness. This figure corresponds to Fig. 4, with the same general view. Panel (a) presents the lift curve slope deviation from 2π, $c_{l,\alpha}/2\pi$. The slope increases as X_{EA} moves backward and exceeds 2π at $X_{EA} \approx 0.45$. Panel (b) presents the aerodynamic center location deviation from the quarter chord, $x_{EA}/(c/4)$. The values are smaller than 100%, i.e., chord-wise elasticity brings the aerodynamic center forward. Unlike the results in Fig. 4b, for $X_{EA} \to 1$ the values do not sharply decrease.

as X_{EA} moves backward, but here it exceeds 2π at $X_{EA} \approx 0.45$. Panel (b) presents the aerodynamic center location deviation from quarter chord, $x_{EA}/(c/4)$. Here again, the values are smaller than 100%, i.e., chord-wise elasticity brings the aerodynamic center forward. Nevertheless, unlike the results in Fig. 4, the strong gradients for $X_{EA} > 0.85$ do not appear here,

Appendix D. The numerical model used in Section 3.5

In the limit of negligible airfoil twist, we used a NACA-2412 airfoil geometry with a chord of $c = 1$ [m], clamped at $x_{EA} = 0.25c$. Young's modulus is $E = 8$ [MPa]. Fluid density is $\rho_\infty = 1.006$ $[\text{kg/m}^3]$ (taken from the standard atmosphere model for an altitude of 2 [km]). The angle-of-attack is $\alpha = 5$ [°], and the uniform potential flow velocity is $u_\infty = 40$ [m/s].

The arbitrarily chosen actuation method used here is known as embedded-fluidic-networks (EFN). A description of the relation between the function d_a, internal pressure, and chambers geometry, is presented in (Matia and Gat, 2015) as a

long-wave approximation by which

$$\frac{\mathrm{d}^2 d_a}{\mathrm{d}x^2} = \phi(x)\psi\,(p_c, x)\,, \tag{D.1}$$

where $\phi(x)$ represents channel density ($1/\phi(x)$ is the distance between the channels) and $\psi\,(p_c, x)$ is the total change in slope $\mathrm{d}d_a/\mathrm{d}x$ due to the actuated channel, where p_c is the pressure within the channels. In the presented calculations, the channel cross-section is a circle of diameter of $h/5$ with the center located $2h/7$ above the midplane, where $h = h(x)$ is the local thickness of the airfoil. For the above parameters and the limit of $p_c/E \ll 1$, ψ is approximated as $\psi \approx 0.1741\,(p_c/E)$ (see Matia and Gat, 2015 for detailed description).

The numerical calculations utilized COMSOL Multiphysics'® Fluid–Structure Interaction (FSI) module, with a grid consisting of 10^3 first-order unstructured triangular elements with average element quality of 0.94 for the fluidic domain and 10^3 second-order unstructured triangular elements with average element quality of 0.9 for the solid domain. The size of the rectangular domain was $8c \times 10c$, rotated by α, so the velocity condition at the front boundary is perpendicular to the boundary. The model included 10^4 degrees of freedom. All our solutions converged by at least six orders of magnitude from the value given at the initial condition. In the first step, the solver created the flow field, allowing deformations to be created and become stable. Then, the internal pressure was applied within the chambers in the second step.

Fig. 5 presents a comparison between analytic and numerical results. Panel (a) compares the difference between the numerical calculation w_n and the analytic results w_a computed by the asymptotic scheme (11) & (12) for uniformly distributed actuation of $\mathrm{d}^2 d_a/\mathrm{d}x^2 = 1.94$. The channel distribution is presented at the insert, where the channels are pressurized at $p_c = 150$ [kPa].

Panels (b) and (c) in Fig. 5 present a comparison between numerical and analytic results by inverse calculations, described in Section 3.5. Panel (b) presents deformation cancellation, which determines the required actuation, and, thus, the geometry of the chambers (see insert in panel (b); channels are pressurized at $p_c = 146$ [kPa]). Panel (c) presents comparisons for the transformation of NACA-2412 camber to NACA-4412 camber (channels are pressurized at $p_c = 896$ [kPa]).

References

Alben, S., 2008. The flapping-flag instability as a nonlinear eigenvalue problem. Phys. Fluids 20, 104106. http://dx.doi.org/10.1063/1.3000670.

Alben, S., 2015. Flag flutter in inviscid channel flow. Phys. Fluids 27, 33603.

Barbarino, S., Bilgen, O., Ajaj, R.M., Friswell, M.I., Inman, D.J., 2011. A review of morphing aircraft. J. Intell. Mater. Syst. Struct. 22, 823–877.

Buoso, S., Palacios, R., 2015. Electro-aeromechanical modelling of actuated membrane wings. J. Fluids Struct. 58, 188–202.

Dowell, E.H., 1974. Aeroelasticity of Plates and Shells. Springer Science & Business Media.

Dowell, E.H., Clark, R., Cox, D., Curtiss, H.C.J., E, J.W., H, K.C., P, D.A., S, R., S, E., S, F., S, T.W., 2005. A Modern Course in Aeroelasticity. In: Solid Mechanics and its Applications.

Eloy, C., Lagrange, R., Souilliez, C., Schouveiler, L., 2008. Aeroelastic instability of cantilevered flexible plates in uniform flow. J. Fluid Mech. 611, 97–106.

Gilmanov, A., Le, T.B., Sotiropoulos, F., 2015. A numerical approach for simulating fluid structure interaction of flexible thin shells undergoing arbitrarily large deformations in complex domains. J. Comput. Phys. 300, 814–843.

Gurugubelli, P.S., Jaiman, R.K., 2015. Self-induced flapping dynamics of a flexible inverted foil in a uniform flow. J. Fluid Mech. 781, 657–694.

Johnston, C.O., 2004. Review, Extension, and Application of Unsteady Thin Airfoil Theory. CIMSS Report.

Kim, D., Cossé, J., Huertas-Cerdeira, C., Gharib, M., 2013. Flapping dynamics of an inverted flag. J. Fluid Mech. 736.

MacPhee, D.W., Beyene, A., 2016. Fluid–structure interaction analysis of a morphing vertical axis wind turbine. J. Fluids Struct. 60, 143–159.

Manela, A., Howe, M.S., 2009. The forced motion of a flag. J. Fluid Mech. 635, 439–454.

Matia, Y., Gat, A.D., 2015. Dynamics of elastic beams with embedded fluid-filled parallel-channel networks. Soft Robot. 2, 42–47.

Moosavian, A., Chae, E.J., Pankonien, A.M., Lee, A.J., Inman, D.J., 2017. A parametric study on a bio-inspired continuously morphing trailing edge. In: Bioinspiration, Biomimetics, and Bioreplication 2017. 1016204.

Mougel, J., Doaré, O., Michelin, S., 2016. Synchronized flutter of two slender flags. J. Fluid Mech. 801, 652–669.

Nguyen, N., Ting, E., Lebofsky, S., 2015. Aeroelastic analysis of a flexible wing wind tunnel model with variable camber continuous trailing edge flap design. In: 56th AIAA/ASCE/AHS/ASC Structures, Structural Dynamics, and Materials Conference.

Païdoussis, M.P., Price, S.J., Langre, E. de, 2010. Fluidelastic instabilities in cylinder arrays. In: Fluid-Structure Interactions. Cambridge University Press, pp. 215–290. http://dx.doi.org/10.1017/CBO9780511760792.006.

Sader, J.E., Cossé, J., Kim, D., Fan, B., Gharib, M., 2016a. Large-amplitude flapping of an inverted flag in a uniform steady flow – a vortex-induced vibration. J. Fluid Mech. 793, 524–555. http://dx.doi.org/10.1017/JFM.2016.139.

Sader, J.E., Huertas-Cerdeira, C., Gharib, M., 2016b. Stability of slender inverted flags and rods in uniform steady flow. J. Fluid Mech. 809, 873–894. http://dx.doi.org/10.1017/JFM.2016.691.

Takahashi, H., Yokozeki, T., Hirano, Y., 2016. Development of variable camber wing with morphing leading and trailing sections using corrugated structures. J. Intell. Mater. Syst. Struct. 27, 2827–2836.

Tang, D.M., Dowell, E.H., 2018. Aeroelastic response and energy harvesting from a cantilevered piezoelectric laminated plate. J. Fluids Struct. 76, 14–36.

Thill, C.L., Etches, J., Bond, I., Potter, K., Weaver, P., 2008. Morphing skins. Aeronaut. J. 112, 117–139.

Tiomkin, S., Raveh, D.E., 2017. On the stability of two-dimensional membrane wings. J. Fluids Struct. 71, 143–163.